# From Waste-Heat Recovery to Refrigeration: Compositional Tuning of Magnetocaloric $Mn_{1+x}Sb$

Joya A. Cooley,  $^{\dagger}$  Matthew K. Horton,  $^{\ddagger}$  Emily E. Levin,  $^{\dagger}$ ,  $^{\P}$  Saul H. Lapidus,  $^{\S}$  Kristin A. Persson,  $^{\ddagger,\parallel}$  and Ram Seshadri\*,  $^{\dagger,\P}$ ,  $^{\bot}$ 

†Materials Research Laboratory, University of California, Santa Barbara California 93106, United States

‡Energy Storage and Distributed Resources Division, Lawrence Berkeley National Laboratory

Berkeley, California 94720, United States

¶Materials Department, University of California, Santa Barbara California 93106, United States

§X-ray Sciences Division, Argonne National Laboratory Lemont, Illinois 60439, United States

||Materials Science and Engineering, University of California, Berkeley
California 94720, United States

⊥Department of Chemistry and Biochemistry, Santa Barbara
California 93106, United States

E-mail: seshadri@mrl.ucsb.edu

#### Abstract

Magnetic refrigeration, as well as waste-heat recovery, can be accomplished through the magnetocaloric effect, where temperature changes the magnetic state of a material or vice versa. Promising magnetocaloric materials display large changes in magnetic entropy ( $\Delta S_M$ ) upon application of a moderate magnetic field, and often associated with magnetic materials possessing some degree of magnetostructural coupling. In such compounds, the magnetic transition is coupled to some structural transition at the ordering temperature, and indicators for these are readily calculated by the magnetic deformation proxy  $\Sigma_M$ . MnSb, with a Curie temperature  $T_C = 577 \, \mathrm{K}$ is has a calculated magnetic deformation of  $\Sigma_M$  = 5.9%, and is a promising candidate material for waste-heat recovery. The temperature-dependence of structural, magnetic, and magnetocaloric properties of  $Mn_{1+x}Sb$ , where x is a tunable amount of interstitial Mn, are studied here. Excess Mn is incorporated as an interstitial whose magnetic moment is anti-aligned with the stoichiometric Mn, and the excess Mn has the effect of lowering  $T_C$ , such that the Curie temperature can be tuned from 577 K to nearly room temperature at 318 K for x = 0.2. For x = 0.0, 0.1, and 0.2, values of  $\Delta S_M$  under a maximum magnetic field H = 5 T are found to be  $3.65 \text{ J K}^{-1} \text{ kg}^{-1}$ ,  $3.00 \text{ J K}^{-1} \text{ kg}^{-1}$ , and 2.83  $\rm J\,K^{-1}\,kg^{-1}$ , respectively. While the maximum  $\Delta S_M$  decreases with x, the high refrigerant capacity — a more holistic measure of performance — is retained in this highly tunable system.

#### Introduction

Continued efforts to decrease energy use and recover waste heat have led to a focus on magnetocaloric materials, which are promising in applications ranging from magnetic refrigeration <sup>1,2</sup> to waste-heat recovery. <sup>3</sup> Key to these applications is the magnetocaloric effect (MCE) where a change in applied magnetic field induces a reversible change in temperature. With appropriate cycling, refrigeration becomes possible. This application has been studied and applied at cryogenic temperatures and at room temperature for refrigeration purposes.<sup>2</sup> The complementary process, termed the reverse MCE, is when changing temperature induces changes in the magnetic state. The reverse MCE can be harnessed into useful mechanical or electrical energy.<sup>2</sup> An important figure of merit governing the performance of magnetocaloric materials is the entropy change due to magnetization  $\Delta S_M$ . Since  $\Delta S_M$  is maximized near  $T_C$ , the ability to tune  $T_C$ , and thus the temperature at which a material is most effective, is valuable from an applications standpoint. Rare-earth free<sup>4</sup> compounds and those not containing toxic elements<sup>5-9</sup> are particularly appealing. Research in the last few decades has focused extensive efforts solid-state refrigeration devices using the Peltier effect as well as thermal energy harvesting technologies such as thermoelectrics using the Seebeck effect, 10 pyroelectrics, 11,12 thermoelastics, 13 and thermomagnetics using the reverse magnetocaloric effect (MCE). <sup>14</sup> A review comparing these different strategies has appeared recently. 15 While the MCE has long been studied for refrigeration and cryogenic cooling, it has been proposed that the reverse MCE for the recovery of low grade heat is a viable option.<sup>3</sup>

In the search for useful magnetocaloric materials, we have employed a previously described computational proxy for the degree of magnetostructural coupling in a material, the magnetic deformation  $\Sigma_M$  which correlates well with  $\Delta S_M$ . <sup>16,17</sup> Using this descriptor and a recently developed workflow for the magnetic properties of materials <sup>18</sup> on materials in the Materials Project, <sup>19</sup> we show that MnSb may be a good magnetocaloric material as indicated by its calculated magnetic deformation,  $\Sigma_M = 5.87\%$ , which is well above the

threshold for remarkable magnetocalorics of 1.5% mentioned by Bocarsly et al. <sup>16</sup> This follows the trend suggested by binary compounds of transition metals and metalloids in the NiAs structure type, which show a host of types of magnetic ordering and varying degrees of magnetostructural coupling. It is well known that this compound exists as  $Mn_{1+x}Sb$ , where x indicates the amount of excess Mn hosted on an interstitial site. Under extreme conditions, x has been found to reach up to 0.5, <sup>20</sup> but using conventional preparation conditions, x ranges between 0.02 and 0.25. <sup>21</sup> Most pertinent to the present study, the amount of interstitial Mn greatly affects the structure and magnetic properties, and can be used to tune  $T_C$  in a predictable way. Okita et al. have proposed that the equation  $T_C = (577 - 790 \times x)$  accounts for the behavior of  $T_C$  with respect to the amount of interstitial Mn, x, in the structure. <sup>21,22</sup>

In this work, we present a study of the magnetocaloric performance of  $\mathrm{Mn}_{1+x}\mathrm{Sb}$  with nominal x values 0.0, 0.1, and 0.2. We are able to exhibit control over  $T_C$  and, in turn, the temperature of the maximum  $|\Delta S_M|$ . While it is unlikely that  $T_C$  control is simply due to the unit cell volume change,  $^{23}$  we suggest the decrease in  $T_C$  is attributable to increased magnetic disorder in the lattice. Density functional theory calculations suggest that the lowest energy configurations correspond to the interstitial Mn moments antiparallel to the principal Mn moments. The magnitude of  $\Delta S_M$  decreases as x increases, but we show that the refrigerant capacity remains robust at all doping levels. Furthermore, we suggest that while maximum  $\Delta S_M$  decreases with increasing interstitial concentration, this is entirely predictable based on the decreasing  $|\Sigma_M|$  value, suggesting that the degree of magnetostructural coupling changes as as interstitial inclusion is increased. The high  $\Delta S_M$  and  $T_C$  tunability make this series uniquely interesting for both magnetic refrigeration and waste-heat recovery applications.

#### **Materials and Methods**

**Synthesis** Polycrystalline powders of  $Mn_{1+x}Sb$  were prepared using a one-step solid state synthesis. Elemental Mn (99.95%, Alfa Aesar) was purified before synthesis by annealing overnight sealed in an evacuated fused silica tube at 1273 K. Purified Mn was then ground and combined with Sb powder ground from shot (99.999%, Alfa Aesar) according to the targeted stoichiometry (e.g.  $Mn_{1.1}Sb$  measured as 1.1 mole Mn and 1.0 mole Sb) to total masses of 0.50 g to 0.75 g. Pre-weighed Mn and Sb powders were combined, ground in an agate mortar and pestle, and pelletized into 6 mm pellets. Pellets were placed in boron nitride crucibles, sealed in evacuated fused silica ampoules, and annealed at 1123 K for 48 h before the furnace was turned off and allowed to cool. For clarity, samples will be referred to according to their nominal Mn compositions (i.e. x = 0.0, 0.1, and 0.2).

Structural characterization High-resolution synchrotron powder X-ray diffraction (XRD) data were collected at room temperature on samples of  $\mathrm{Mn_{1+x}Sb}$ , x=0, 0.1, and 0.2, and at several temperatures above and below  $T_C$  on x=0.0 using the dedicated hot gas blower at beamline 11-BM at the Advanced Photon Source (APS), Argonne National Laboratory. For room temperature scans, powderized samples were loaded into a 0.8 mm diameter Kapton capillary and measured for one hour with  $\lambda=0.412801\,\mathrm{\mathring{A}}$ . For high temperature measurements of x=0.0, the sample was loaded into a a 1.1 mm diameter fused silica capillary, sealed on each end with clay, and measured with  $\lambda=0.412825\,\mathrm{\mathring{A}}$ . During the multi-temperature measurement, temperature was swept at 0.5 K min<sup>-1</sup> while collecting 10 min scans between  $0.00\,^{\circ}2\theta$  and  $6.00\,^{\circ}2\theta$  (Q approximately ranging from  $0.13\,\mathrm{\mathring{A}}^{-1}$  to  $7.35\,\mathrm{\mathring{A}}^{-1}$ ), such that each scan encompasses approximately 5 K. Rietveld refinements of data were performed using TOPAS and structures visualized using VESTA-3. <sup>24</sup> Scanning electron microscopy was conducted using an Apreo C (FEI) at 20 keV. Energy dispersive X-ray spectroscopy (EDS) was used to locally measure compositions of powders.

Magnetic measurements Magnetic properties were measured on 5 mg to 15 mg pieces of annealed pellets using a Quantum Design MPMS3 SQUID vibrating sample magnetometer (VSM). Pieces of each sample were attached to the Quantum Design oven stick, capable of high temperature measurements, with Zircar cement, and cured with a heat gun for 30 s to 1 min. Because of the lower  $T_C$  of x=0.2, this sample was measured in a VSM powder sample holder using chamber temperature control. Zero field— and field—cooled magnetization (M) vs temperature (T) measurements were taken upon warming at a rate of  $7 \, \mathrm{Kmin}^{-1}$ . Arrott plots were constructed with one quadrant of M vs applied field (H) measurements (i.e.,  $0 \, \mathrm{T}$  to  $5 \, \mathrm{T}$ ) at  $3 \, \mathrm{K}$  intervals above and below the approximate  $T_C$ ; details for each composition can be found in the Supporting Information (Figures S4–S6). In order to determine  $\Delta S_M$ , M versus T measurements were taking on cooling (using a rate of  $5 \, \mathrm{K\,min}^{-1}$ ) at various fields from  $H=0.1 \, \mathrm{T}$  to  $H=5 \, \mathrm{T}$ . Further details of  $\Delta S_M$  calculations have been reported elsewhere, and Python code to calculate magnetic entropy changes is from Bocarsly et al.  $^{25}$ 

Electronic structure calculations Previous work established  $\Sigma_M$  as a descriptor for magnetocaloric materials, whereby a structural relaxation was performed within conventional density functional theory (DFT) for a given crystal structure initialized in both a ferromagnetic order and also in non-spin-polarized configuration where magnetic moments are constrained to be zero. This latter case, though an idealized configuration and not directly comparable to a paramagnetic state, is sufficient to capture a measure of magnetostructural coupling through a comparison of the equilibrium lattice parameters in both cases, and this was found to correlate well to  $\Delta S_M$ . A high-throughput screening of inorganic materials sourced from the Materials Project<sup>19</sup> revealed that MnSb was one such material with a  $\Sigma_M$  of 5.87% significantly higher than the 1.5% cut-off proposed for promising magnetocalorics. <sup>16</sup>

All DFT calculations were performed using the Vienna Ab initio Simulation Package 26

and using standard settings suggested by the atomate  $^{27}$  software package and also its workflows for magnetic materials,  $^{18}$  including projector augmented wave pseudopotentials with Mn including 3p, 3d and 4s electrons as valence, a plane-wave cut-off of 520 eV, and a k-point density of at least 64 k-points  $\mathring{A}^{-3}$ . For calculation of magnetic deformations, two approaches were attempted. The first in which all Mn atoms were initialized in a ferromagnetic configuration, and another where the host Mn atoms were initialized in a ferromagnetic configuration but the Mn interstitial atoms initialized with anti-parallel spin for an overall ferrimagnetic ordering. While both configurations produced qualititively similar trends, the results reported here are for the more physical and lower-energy ferrimagnetic orderings.

The DFT method cannot simulate disordered cells so ordered approximations were constructed for the intermediate compositions containing interstitial Mn using the pymatgen <sup>28</sup> package. For each composition, three separate ordered approximations were taken with cells containing approximately fifty atoms, and the magnetic deformation calculated for each and their means reported. For each composition, the difference in magnetic deformation between different ordered approximations was low, with 4.21 %, 4.49 % and 4.75 % for x = 0.1 and 3.68 %, 3.74 % and 3.78 % for x = 0.2, so this approximation was considered sufficient for establishing the expected trends in magnetic deformation as interstitial content was increased.

#### Results and discussion

#### Structural characterization

The hexagonal unit cell of MnSb in the NiAs ( $P6_3/mmc$ , No. 194) structure type is pictured in Figure 1(a), with the pseudo-octahedral coordination environment of Mn (2a site) emphasized. Figure 1(b) depicts the same view of the unit cell, but with the trigonal bipyramidal coordination of the partially occupied interstitial Mn position (2d site) empha-

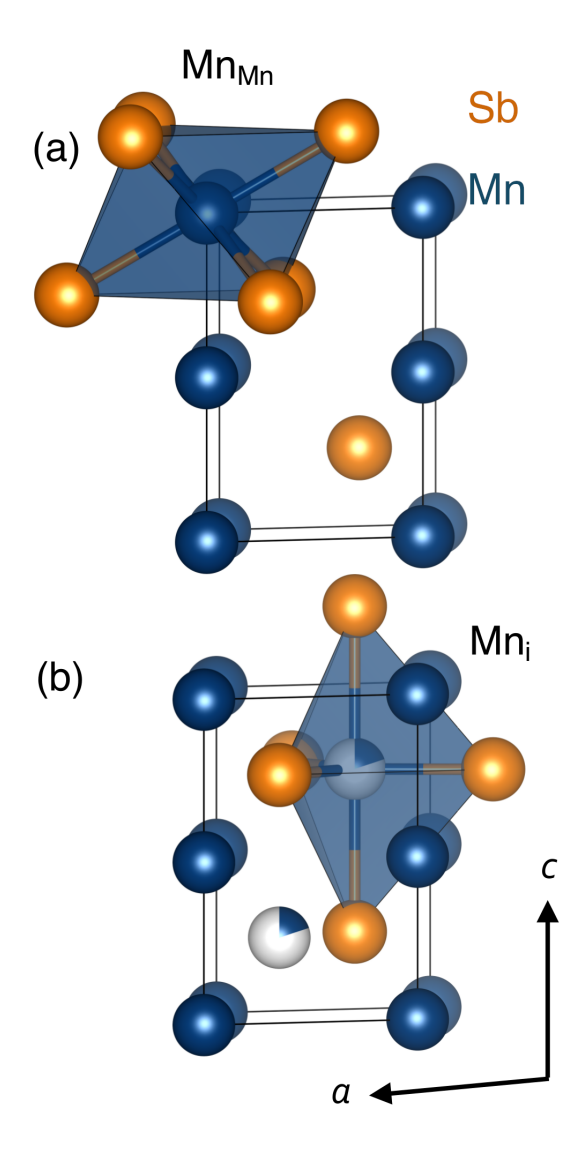


Figure 1: (a) One unit cell of stoichiometric MnSb is depicted with the octahedral coordination of the  $\mathrm{Mn}_{Mn}$  site emphasized. (b) The unit cell is shown including the coordination of partially occupied  $\mathrm{Mn}_i$  site with trigonal bipyramidal coordination.

sized. We employ the Kröger-Vink notation and refer to the stoichiometric Mn position as  $Mn_{Mn}$  and interstitial position as  $Mn_i$ . It is worth noting that the partial occupation of the  $Mn_i$  position results in the  $Ni_2$ In structure type where the 2d site is partially occupied.

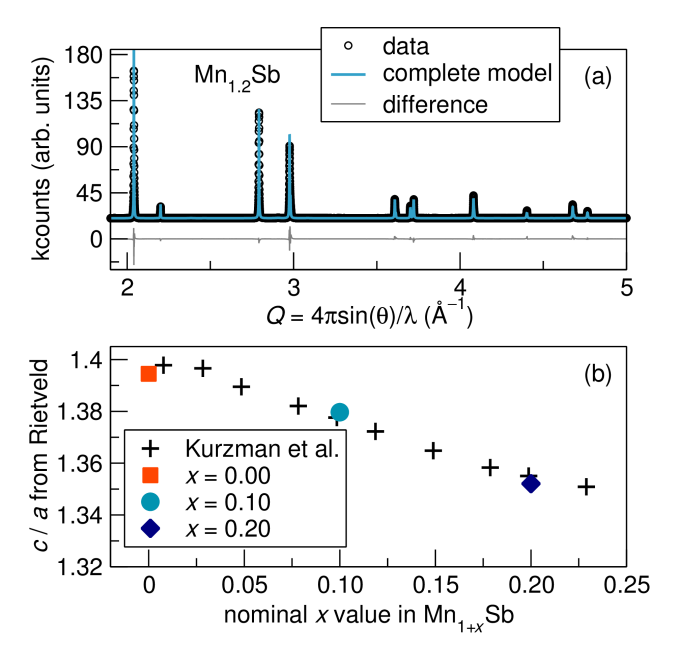


Figure 2: (a) Room–temperature synchrotron X-ray diffraction data fit to the hexagonal MnSb structure and the tetragonal Mn<sub>2</sub>Sb structure (2.4 wt%). (b) c/a ratio as determined by Rietveld refinement of X-ray diffraction data (closed symbols) compared to literature values (plus signs, from Kurzman et al<sup>29</sup>) showing a decreasing trend.

Figure 2(a) shows a representative Rietveld refinement of synchrotron X-ray diffraction data for x = 0.2. Full diffraction patterns with individual contributions from each phase for each sample (Figs. S1-S3) and data from Rietveld refinement (Table S2) can be found in the Supporting Information. In each sample, the major phase is MnSb, yet there is some degree of sample inhomogeneity. To fit shouldered peaks properly, a second MnSb phase with a slightly larger unit cell volume, suggesting a slightly higher  $Mn_i$  content, can be fit to the pattern, and this has previously been shown to occur in CrTe which is also in the NiAs structure type. <sup>30</sup> Because of the degree of peak overlap between these phases, an approximate  $Mn_i$  composition as determined by Rietveld refinement is unreliable, but this did not interfere with reliable determination of unit cell parameters of the main phase. Several other methods of confirming increasing interstitial inclusion are discussed below.

The stoichiometric x=0 compound has proven difficult to synthesized precisely, and measurements on single-crystals show some degree of interstitial composition, even when the stoichiometric phase is targeted.<sup>21</sup>

In addition, x=0.0 contains a small amount (<1%) of elemental Sb, however this is unlikely to affect measured magnetic properties and magnetocaloric performance as Sb exhibits no magnetic ordering under these measurement conditions. x=0.2 is near the Mn solubility limit and shows formation of Mn<sub>2</sub>Sb (P4/nmm, No. 129), a ferrimagnet found to order near 550 K,<sup>31</sup> and the formation of this impurity is also seen in single crystal growth.<sup>32</sup> Although this particular impurity phase is magnetic, its high ordering temperature as compared to x=0.2 (discussed later) implies it should have a negligible effect on the measurement of magnetocaloric performance of x=0.2. However, it is not certain that the impurity phase has no influence on the magnetic entropy change without comparison to behavior of a pure sample, but mention here that there is a very small amount (2.4 wt% from Rietveld refinement of synchrotron X-ray diffraction data) of the Mn<sub>2</sub>Sb impurity.

As previously discussed, occupation of the  $\mathrm{Mn}_i$  position increases the a lattice parameter while decreasing the c lattice parameter, resulting in an overall increase in unit cell volume and decrease in the c/a ratio. Kurzman et al. systematically studied the c/a ratio decrease as a function of nominal composition through refinement of both high-resolution synchrotron powder diffraction and pair distribution function measurements, which agreed well with one another. <sup>29</sup> In Figure 2(b), the c/a ratios derived from Rietveld refinement of synchrotron data (closed symbols) are compared to the Kurzman data (open symbols) and show excellent agreement. These data are thus a good indicator that the  $\mathrm{Mn}_i$  position is increasingly being occupied. To understand local composition, EDS was employed and also showed increasing Mn incorporation (data in Table S1 of the Supporting Information).

#### Temperature-dependent structure

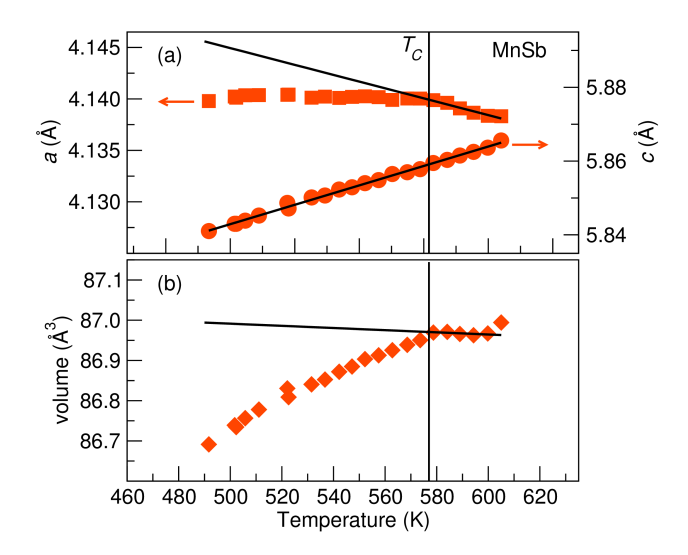


Figure 3: (a)Temperature-dependent lattice parameters a (squares, left axis) and c (circles, right axis) and (b) unit cell volume derived from Rietveld refinement of temperature-dependent synchrotron X-ray diffraction data on x=0.0. In both panels, the solid vertical line is the approximate  $T_C$ , and the sloped lines indicate the best linear fit to paramagnetic (i.e. above  $T_C$ ) unit cell parameter data. In both panels, error bars are smaller than data markers.

Figure 3 shows the dependence of the unit cell parameters (a) a(=b) and c as well as (b) the unit cell volume (as determined by Rietveld refinement) on temperature as heated through  $T_C$  in x=0.0. It is clear that the temperature dependence of the c parameter does not change significantly throughout the temperature range measured here. However, the a parameter exhibits negative thermal expansion (NTE) above  $T_C$ , then shows a noticeable change in slope near 575 K, very near to  $T_C$ . Below  $T_C$ , the temperature dependence of the a axis resembles an Invar effect, where thermal expansion becomes invariant below  $T_C$ ,  $T_C$  and  $T_C$  but is not observed in the  $T_C$  direction. The shift in slope is also quite prominent in the temperature dependent unit cell volume, where above  $T_C$  the slope is  $T_C$ 0 and shifts to  $T_C$ 1. As was predicted by the magnitude of  $T_C$ 2, we clearly observe a change in the coefficient of thermal expansion manifesting itself as negative spontaneous volume magnetostriction ( $T_C$ 1) near the expected  $T_C$ 2.  $T_C$ 3 can be quantified according to the following equation:  $T_C$ 34,35

$$\omega_V(T) = \frac{(V - V_{\rm p})}{V_{\rm p}} \tag{1}$$

where V is the experimental value of the unit cell volume at a temperature, T, and  $V_{\rm p}$  is unit cell volume calculated from extrapolating the temperature dependence in the paramagnetic state (above  $T_C$ ) to temperature T. For x=0,  $\omega_V=-0.003$  at 490 K, which clearly confirms a negative spontaneous volume magnetostriction. Many Mn-based magnets show positive spontaneous volume magnetostriction at the Curie or Neèl temperature, such as LaMnO<sub>3</sub>,  $^{36}$  MnAs,  $^{37}$  YMn $_2$   $^{38}$  as well as several Mn-based compounds in the Ni $_2$ In structure type.  $^{39}$  However negative volume magnetostriction is not unprecedented in Mn-based materials and both MnO and MnS exhibit it at their Neèl temperatures.  $^{40}$ 

The overall results are in agreement with the original reports on this material which also show the temperature dependence of c to be linear between 300 K and 770 K, but show a discontinuity in the a direction near  $T_C$ .<sup>41</sup> The previous results also suggest that the anomalous thermal expansion below  $T_C$  (manifesting as NTE in the present work) resembles a type of electronic NTE mechanism. Through this mechanism, on either side of the phase transition, the material exhibits conventional positive thermal expansion (PTE), but in some region where there is crossover between two phases (e.g., a non-magnetic and magnetic phase), NTE occurs. 42 While the results of Willis et al. are in good agreement with this mechanism, the results of the present work are somewhat inconsistent with this mechanism. In this work, NTE actually occurs before the expected paramagneticto-ferrimagnetic phase transition, in the region where phase-crossover is not necessarily expected. Additionally, Willis et al. show that the thermal expansion anomaly appears more like near-zero thermal expansion (NZTE) in the crossover region, and is sustained over nearly 100 K, however the data density is low (4 data points over a 100 K range). The precise details, and perhaps elucidation of the mechanism driving the thermal expansion anomaly, could be better understood by acquiring temperature-dependent high-resolution synchrotron X-ray diffraction data at higher temperatures, perhaps above the suggested

crossover region, with higher data density.

#### **Magnetic characterization**

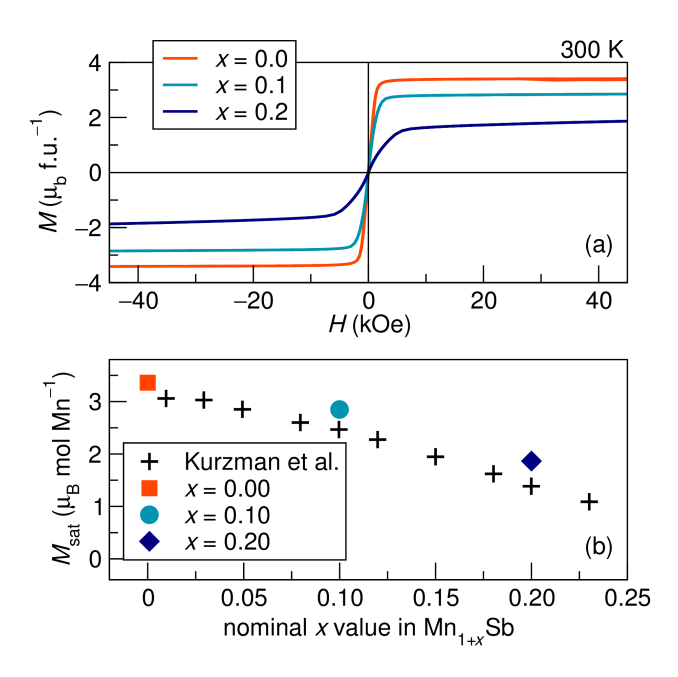


Figure 4: (a) Field–dependent magnetization data at 300 K for x = 0.0, 0.1, and 0.2 showing a decreasing trend in saturation magnetization. (b)  $M_{sat}$  data from field–dependent magnetization measurements for data presented in this work (closed symbols) and previous literature (plus signs, from Kurzman et al.<sup>29</sup>)

Magnetic properties of  $\mathrm{Mn_{1+x}Sb}$  have long been studied, but recently Taylor et al. settled an important debate on whether or not the  $\mathrm{Mn_i}$  possesses a magnetic moment. <sup>23</sup> It has been seen that the inclusion of  $\mathrm{Mn_i}$  decreases the saturation magnetization,  $M_{sat}$ , which can be explained by an antiparallel moment on  $\mathrm{Mn_i}$ . As previously discussed, the antiparallel orientation of the  $\mathrm{Mn_i}$  moment with respect to that of  $\mathrm{Mn_{Mn}}$  is expected to decrease the overall  $M_{sat}$  as  $\mathrm{Mn_i}$  composition increases. Figure 4(a) depicts field–dependent magnetization traces (M vs H) measured at room temperature. Each shows magnetic ordering at relatively low field, and as the nominal excess  $\mathrm{Mn}$  increases the curve saturates at lower values. In Figure 4(b), a comparison between  $M_{sat}$  values vs H for the data measured by Kurzman et al. (plus signs) and present samples (closed symbols) are shown to be in good agreement, further validating increasing interstitial inclusion.

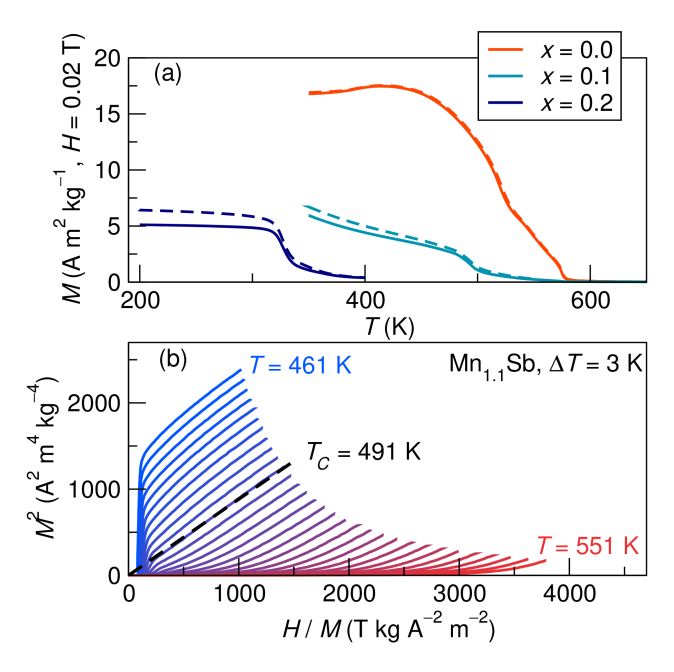


Figure 5: (a) Zero-field-cooled (solid) and field-cooled (dashed) temperature-dependent magnetization data measured using H = 200 Oe for x = 0.0, 0.1, and 0.2. (b) Isothermal field-dependent magnetization scans plotted in the Arrott style for x = 0.1 yields  $T_C \approx 491$  K (predicted as 498 K from  $T_C = (577 - 790 \times x)$ .

Increasing interstitial inclusion decreases  $T_C$ , and Figure 5(a) shows M vs T traces for each sample measured with H=200 Oe. Each sample shows little thermomagnetic irreversibility, consistent with their low coercive fields ( $H_C$ ) at room temperature. Additionally, the transitions from the paramagnetic to ferrimagnetic states clearly occur at decreasing temperatures with increasing  $Mn_i$  composition. While this fits the expected trend, the precise ordering temperatures are difficult to assign due to the broadness of the transitions (likely due to the aforementioned sample inhomogeneity). To assign more precise ordering temperatures, several isothermal M vs H traces were measured for each sample through each approximate  $T_C$ . When these data are plotted in the Arrott format ( $M^2$  vs H/M),  $^{43}$  the isotherm that extrapolates to the origin indicates  $T_C$ . Figure 5(b) shows the Arrott plot representative example, x=0.1, where  $T_C$  is found to be 491 K, which is in good agreement with the experimental  $T_C$  calculated using ( $T_C=577-790\times x$ , 498 K). The agreement is similar for x=0.0 where the experimental  $T_C$  is determined to be 560 K and the calculated  $T_C$  is 577 K (Figure S5 of the Supporting Information). There is a much

larger discrepancy between the experimentally determined (339 K) and calculated (419 K)  $T_C$  values for x = 0.2 (Figure S6 of the Supporting Information) that is as yet unexplained and will require further investigation.

#### Magnetocaloric performance

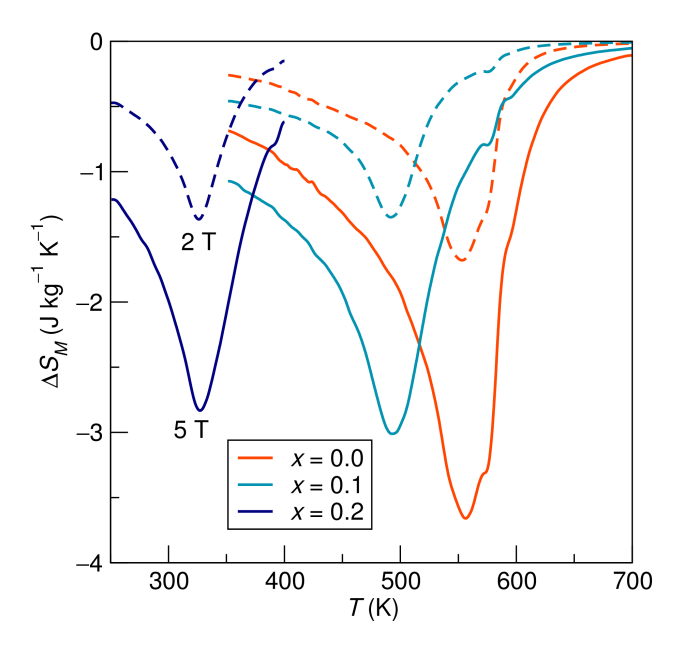


Figure 6: Calculated  $\Delta S_M$  traces for x = 0.0, 0.1, and 0.2 for select field changes.

In order to calculate  $\Delta S_M$ , temperature-dependent magnetization was measured through  $T_C$  at varying fields, derived, and integrated over field to produce the  $\Delta S_M$  traces shown in Figure 6; the complete sets of M vs. T data, derivative traces, and  $\Delta S_M$  traces for each composition can be found in the Supporting Information (Figures S7–S9). It is clear from the peak of each  $\Delta S_M$  curve that the  $T_C$ , and therefore temperature of maximum magnetocaloric effect decreases as Mn interstitial inclusion increases. In this series,  $\Delta S_M$  values range from 3.65 J K<sup>-1</sup> kg<sup>-1</sup> and 2.83 J K<sup>-1</sup> kg<sup>-1</sup>, decreasing as interstitial inclusion increases. These values are comparable to those of other compounds exhibiting continuous phase transitions at  $T_C$ , which are often in the range of 5 J K<sup>-1</sup> kg<sup>-1</sup> to 10 J K<sup>-1</sup> kg<sup>-1</sup>.

It is also of note that the maximum value of  $\Delta S_M$  decreases slightly as interstitial inclusion increases. Here, we make two comments about the decreasing magnetocaloric

performance, the first being that this decrease is not unexpected based on the computational results. Figure 7(c) and (d) show the computationally derived  $\Sigma_M$  parameter for each composition and experimentally determined maximum  $|\Delta S_M|$ , respectively, for each composition. It is suggested by the decreasing  $\Sigma_M$  values that the degree of magnetostructural coupling decreases as the interstitial is added in such a way that the magnetoelastic transition is somehow lessened, and this is corroborated by the decreasing absolute value of  $\Delta S_M$ .

The second point is that the refrigerant capacity, discussed in the introduction, remains relatively robust, especially between the nominally stoichiometric and x=0.1 samples. Refrigerant capacity was first introduced by Wood et al.<sup>44</sup> and further developed by Gschneider et al.<sup>1</sup> as a measure of the heat transferred between sides in one refrigeration cycle. Refrigerant capacity (RC) can be calculated as

$$RC = \int_{T_{cold}}^{T_{hot}} \Delta S(T, P, \Delta H)_{P, \Delta H} dT$$
 (2)

and the temperature ranges for calculation are as follows: x=0.0, 494 K to 587 K; x=0.1, 415 K to 536 K; x=0.2, 270 K to 365 K. Figures 7(a)—(e) show magnetic and magnetocaloric properties for each sample, including the calculated RC value. The case of RC remaining robust is nicely illustrated in that there is a very clear decrease in the maximum  $\Delta S_M$  from x=0.0 to 0.1 seen in Figure 6. Qualitatively, while the x=0.1  $\Delta S_M$  peak is not as sharp, its FWHM is over a broader temperature range, meaning that although the maximum  $\Delta S_M$  has decreased, the RC remains nearly the same, and actually slightly increases. This indicates the overall performance may not be affected much just based on the simple decrease in maximum  $\Delta S_M$ . The RC value for the x=0.2 sample RC is also still in line with other materials with similar or higher  $\Delta S_M$  values for the same field change.<sup>2</sup>

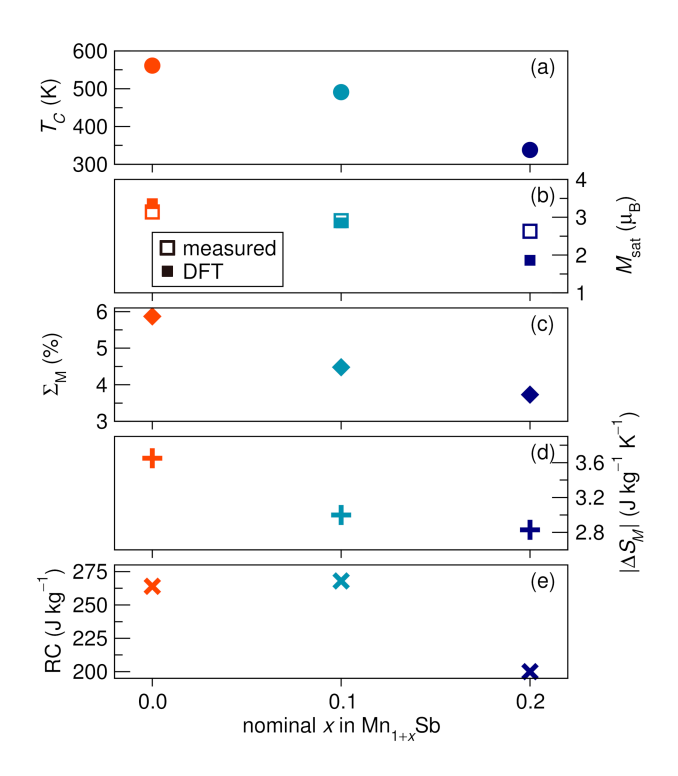


Figure 7: A summary of magnetic and magnetocaloric properties of each sample vs its nominal x value is shown including (a)  $T_C$  from Arrott analysis, (b) the DFT (open symbols) and measured (closed symbols)  $M_{sat}$ , (c) the computed  $\Sigma_M$ , (d) the experimentally determined  $|\Delta S_M|$ , and (e) the refrigerant capacity.

#### Conclusion

In closing, MnSb was proposed as a promising magnetocaloric material as a result of a computational screening on the Materials Project 19 using a previously-described descriptor. 16 MnSb was synthesized with a variety of interstitial content values and  $T_C$  was found to be tunable from high temperatures (561 K) to nearly room temperature (318 K) using interstitial composition (x in Mn<sub>1+x</sub>Sb) as a tuning parameter. The change in magnitude of  $\Delta S_M$  with changing x follows the trend suggested using the DFT-based magnetic deformation proxy  $\Sigma_M$ . Although tuning  $T_C$  down to room temperature causes a decrease in the maximum  $\Delta S_M$ , the refrigerant capacity throughout the series remains robust, suggesting that overall magnetocaloric performance would not be impacted much by x inclusion. Furthermore, the prediction of decreasing  $\Delta S_M$  with increasing x indicates that there is a change in the degree of magnetostructural coupling as the interstitial concentration increases and this may be worthy of further investigation.

**Supporting Information** Details of compositional analysis by EDS, Rietveld refinement, and magnetic properties of all samples; Synchrotron X-ray diffraction data and Rietveld refinements, Arrott Plots, and calculated  $\Delta S_M$  plots

### Acknowledgements

This work was supported by the National Science Foundation (NSF) through This work was supported by the National Science Foundation (NSF) through DMR-SSMC 1710638. The research reported here made use of shared experimental facilities of the NSF Materials Research Science and Engineering Center (MRSEC) at UC Santa Barbara (DMR 1720256). The UCSB MRSEC is a member of the Materials Research Facilities Network (www.mrfn.org). MKH and KAP were supported by the U.S. Department of Energy, Office of Science, Office of Basic Energy Sciences, Materials Sciences and Engineering Division

under Contract No. DE-AC02-05CH11231 (Materials Project program KC23MP). Use of the Advanced Photon Source at Argonne National Laboratory was supported by the U. S. Department of Energy, Office of Science, Office of Basic Energy Sciences, under Contract No. DE-AC02-06CH11357. MKH, KAP, and RS would like to acknowledge BASF for initial support of research into magnetocalorics.

#### References

- (1) Pecharsky, V. K.; Gschneider, Jr., K. A. Some Common Misconceptions Concerning Magnetic Refrigerant Materials. *J. Appl. Phys.* **2001**, *90*, 4614–4622.
- (2) Franco, V.; Blázquez, J.; Ingale, B.; Conde, A. The Magnetocaloric Effect and Magnetic Refrigeration Near Room Temperature: Materials and Models. *Annu. Rev. Mater. Res.* **2012**, *42*, 305–342.
- (3) Kishore, R. A.; Priya, S. Low-Grade Waste Heat Recovery Using the Reverse Magnetocaloric Effect. *Sustainable Energy Fuels* **2017**, *01*, 1–10.
- (4) Brück, E.; Tegus, O.; Thanh, D. T. C.; Trung, N. T.; Buschow, K. H. J. A Review on Mn Based Materials for Magnetic Refrigeration: Structure and Properties. *Int. J. Refrig.* **2008**, *31*, 763–770.
- (5) Tan, X.; Chai, P.; Thompson, C. M.; Shatruk, M. Magnetocaloric Effect in AlFe<sub>2</sub>B<sub>2</sub>: Toward Magnetic Refrigerants from Earth-Abundant Elements. *J. Am. Chem. Soc.* **2013**, *135*, 9553–9557.
- (6) Ren, Q.; Hutchison, W. D.; Wang, J.; Studer, A. J.; Campbell, S. J. Magnetic and Structural Transitions Tuned through Valence Electron Concentration in Magnetocaloric Mn(Co<sub>1-x</sub>Ni<sub>x</sub>Ge). *Chem. Mater.* **2018**, *30*, 1324–1334.

- (7) Hering, P.; Friese, K.; Voigt, J.; Persson, J.; Aliouane, N.; Grzechnik, A.; Senyshyn, A.; Brückel, T. Structure, Magnetism, and the Magnetocaloric Effect of MnFe<sub>4</sub>Si<sub>3</sub> Single Crystals and Powder Samples. *Chem. Mater.* **2015**, *27*, 7128–7136.
- (8) Boeije, M. F. J.; Roy, P.; Guillou, F.; Yibole, H.; Miao, X. F.; Caron, L.; Banerjee, D.; van Dijk, N. H.; de Groot, R. A.; Brück, E. Efficient Room-Temperature Cooling with Magnets. *Chem. Mater.* **2016**, *28*, 4901–4905.
- (9) Liu, J.; Gottschall, T.; Skokov, K. P.; Moore, J. D.; Gutfleisch, O. Giant Magnetocaloric Effect Driven by Structural Transitions. *Nat. Mater.* **2012**, *11*, 620–626.
- (10) Zhang, X.; Zhao, L.-D. Thermoelectric Materials: Energy Conversion Between Heat and Electricity. *J. Materiomics* **2015**, *1*, 92–105.
- (11) Lang, S. B. Pyroelectricity: From Ancient Curiosity to Modern Imaging Tool. *Phys. Today.* **2005**, *58*, 31–36.
- (12) Hunter, S. R.; Lavrik, N. V.; Mostafa, S.; Rajic, S.; Datskos, P. G. Review of Pyroelectric Thermal Energy Harvesting and New MEMs-Based Resonant Energy Conversion Techniques. *Proc. SPIE* **2012**, *8377*.
- (13) Zhu, J. J.; Liang, N. G.; Liew, K. M.; Huang, W. M. Energy Conversion in Shape Memory Alloy Heat Engine Part I: Theory. *J. Intell. Mater. Syst. Struct.* **2001**, *12*, 127–132.
- (14) Kishore, R. A.; Priya, S. A Review on Design and Performance of Thermomagnetic Devices. *Renewable Sustainable Energy Rev.* **2018**, *81*, 33–44.
- (15) Kishore, R. A.; Priya, S. A Review on Low-Grade Thermal Energy Harvesting: Materials, Methods and Devices. *Materials* **2018**, *11*.

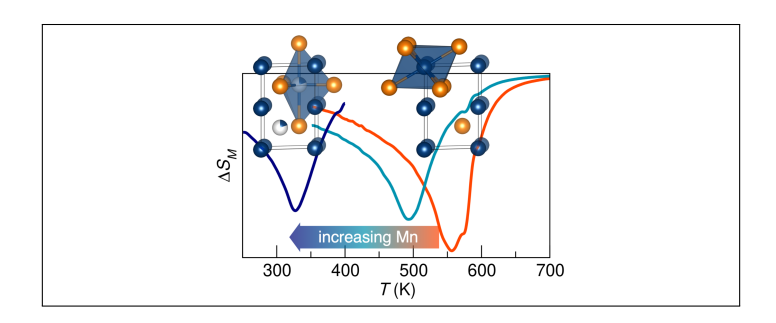
- (16) Bocarsly, J. D.; Levin, E. E.; Garcia, C. A. C.; Schwennicke, K.; Wilson, S. D.; Seshadri, R. A Simple Computational Proxy for Screening Magnetocaloric Compounds. *Chem. Mater.* **2017**, *29*, 1613–1622.
- (17) Bocarsly, J. D.; Levin, E. E.; Humphrey, S. A.; Faske, T.; Donner, W.; Wilson, S. D.; Seshadri, R. Magnetostructural Coupling Drives Magnetocaloric Behavior: The Case of MnB versus FeB. *Chem. Mater.* **2019**, *31*, 4873–4881.
- (18) Horton, M. K.; Montoya, J. H.; Liu, M.; A., P. K. High-Throughput Prediction of the Ground-State Collinear Magnetic Order of Inorganic Materials Using Density Functional Theory. *npj Comput. Mater.* **2019**, *5*.
- (19) Jain, A.; Montoya, J.; Dwaraknath, S.; Zimmermann, N. E. R.; Dagdelen, J.; Horton, M.; Huck, P.; Winston, D.; Cholia, S.; Ong, S. P.; Persson, K. In *Handbook of Materials Modeling: Methods: Theory and Modeling*; Andreoni, W., Yip, S., Eds.; Springer International Publishing: Cham, Switzerland, 2018; pp 1–34.
- (20) Ryzhkovskii, V. M.; Goncharov, V. S. Effect of High-Pressure High-Temperature Processing on the Phase Composition and Magnetic State of  $Mn_{1+x}Sb$  (0  $\leq x \leq 1.0$ ) Alloys. *Inorg. Mater.* **2010**, *46*, 226–231.
- (21) Okita, T.; Makino, Y. Crystal Magnetic Anisotropy and Magnetization of MnSb. *J. Phys. Soc. Jpn.* **1968**, *25*, 120–124.
- (22) Yamaguchi, Y.; Watanabe, H.; Suzuki, T. Magnetic Moment of Excess Mn in  $Mn_{1+\delta}Sb$ . *J. Phys. Soc. Jpn.* **1976**, *41*, 703–704.
- (23) Taylor, A. E.; Berlijn, T.; Hahn, S. E.; May, A. F.; Williams, T. J.; Poudel, L.; Calder, S.; Fishman, R. S.; Stone, M. B.; Aczel, A. A.; Cao, H. B.; Lumsden, M. D.; Christianson, A. D. Influence of Interstitial Mn on Magnetism in the Room-Temperature Ferromagnet Mn<sub>1+δ</sub>Sb. *Phys. Rev. B* **2015**, *91*, 224418.

- (24) Momma, K.; Izumi, F. VESTA 3 for Three-Dimensional Visualization of Crystal, Volumetric and Morphology Data. *J. Appl. Cryst.* **2011**, *44*, 1272–1276.
- (25) Bocarsly, J. D.; Need, R. F.; Seshadri, R.; Wilson, S. D. Magnetoentropic Signatures of Skyrmionic Phase Behavior in FeGe. *Phys. Rev. B* **2018**, *97*, 100404.
- (26) Kresse, G.; Furthmüller, J. Efficient Iterative Schemes for *ab initio* Total-Energy Calculations Using a Plane-Wave Basis Set. *Phys. Rev. B* **1996**, *54*, 11169–11186.
- (27) Mathew, K. et al. Atomate: A High-Level Interface to Generate, Execute, and Analyze Computational Materials Science Workflows. *Comput. Mater. Sci.* **2017**, *139*, 140–152.
- (28) Ong, S. P.; Richards, W. D.; Jain, A.; Hautier, G.; Kocher, M.; Cholia, S.; Gunter, D.; Chevrier, V. L.; Persson, K. A.; Ceder, G. Python Materials Genomics (pymatgen): A Robust, Open-Source Python Library for Materials Analysis. *Comput. Mater. Sci.* 2013, 68, 314–319.
- (29) Kurzman, J. A.; Martinolich, A. J.; Neilson, J. R. Influence of Interstitial Mn on Local Structure and Magnetism in  $Mn_{1+\delta}Sb$ . *Phys. Rev. B: Condens. Matter Mater. Phys.* **2015**, *92*, 1–10.
- (30) Gordienko, V. A.; Zubenko, V. V.; Nkolaev, V. I. Spontaneous Magnetostriction of CrTe. *J. Exp. Theor. Phys.* **1970**, *30*, 864–865.
- (31) Anand, K.; Christopher, N.; Kumar, J.; Gupta, A.; Singh, N. Coercivity Enhancement and Magnetic Property Evaluation of Bi Doped Mn<sub>2</sub>Sb. *J. Magn. Magn. Mater.* **2019**, 476, 29–34.
- (32) Chen, T.; Charlan, G. B.; Keezer, R. C. Growth of MnSb Single Crystals by Pulling With a Seed from Nonstoichiometric Molten Solution. *J. Cryst. Growth* **1977**, *37*, 29–36.

- (33) Nakamura, Y. The Invar Problem. *IEEE Trans. on Magn.* **1976**, *12*, 278–291.
- (34) Kusz, J.; Juszczyk, S.; Warczewski, J. An X-ray Diffraction Study of Magnetostriction in  $Zn_{1-x}Cu_xCr_2Se_4$  (0.2 < x < 1.0). *J. Appl. Crystallogr.* **1988**, *21*, 898–901.
- (35) Bombik, A.; Böhm, H.; Kusz, J.; Pacyna, A. W. Spontaneous Magnetostriction and Thermal Expansibility of TmFeO<sub>3</sub> and LuFeO<sub>3</sub> Rare Earth Orthoferrites. *J. Magn. Magn. Mater.* **2001**, *234*, 443–453.
- (36) Kadomtseva, A. M.; Popov, Y. F.; Vorob'ev, G. P.; Kamilov, K. I.; Ivanov, V. Y.; Mukhin, A. A.; Balbashov, A. M. Thermal-Expansion and Magnetostriction Anomalies in Phase Transitions in  $La_{1-x}Sr_xMnO_3$ . *Phys. Solid State* **2000**, *42*, 1110–1115.
- (37) Chernenko, V. A.; Wee, L.; McCormick, P. G.; Street, R. Giant Magnetoelastic Response in MnAs. *J. Appl. Phys.* **1999**, *85*, 7833–7837.
- (38) Shiga, M.; Wada, H.; Nakamura, Y. Magnetism and Thermal Expansion Anomaly of RMn<sub>2</sub> (R=Y, Gd, Tb, Ho and Er). *J. Magn. Magn. Mater.* **1983**, *31-34*, 119–120.
- (39) Hu, F.; Shen, F.; Hao, J.; Liu, Y.; Wang, J.; Sun, J.; Shen, B. Negative Thermal Expansion in the Materials With Giant Magnetocaloric Effect. *Front. Chem.* **2018**, *6*, 438.
- (40) Morosin, B. Exchange Striction Effects in MnO and MnS. *Phys. Rev. B* **1970**, *1*, 236–243.
- (41) Willis, B. T. M.; Rooksby, H. P. Magnetic Transitions and Structural Changes in Hexagonal Manganese Compounds. *Proc. Phys. Soc. B* **1954**, *67*, 290–296.
- (42) Attfield, J. P. Mechanisms and Materials for NTE. Front. Chem. 2018, 6, 371.
- (43) Arrott, A. Criterion for Ferromagnetism from Observations of Magnetic Isotherms. *Phys. Rev.* **1957**, *108*, 1394–1396.

(44) Wood, M. E.; Potter, W. H. General Analysis of Magnetic Refrigeration and its Optimization Using a New Concept: Maximization of Refrigerant Capacity. *Cryogenics* **1985**, *25*, 667–683.

## **Graphical TOC Entry**



## Supporting Information for

### From Waste-Heat Recovery to Refrigeration:

### Compositional Tuning of Magnetocaloric $Mn_{1+x}Sb$

Joya A. Cooley, † Matthew K. Horton, ‡ Emily E. Levin, †, ¶ Saul H. Lapidus, § Kristin A. Persson, ‡,  $\parallel$  and Ram Seshadri\*, †,  $\P$ ,  $\perp$ 

†Materials Research Laboratory, University of California, Santa Barbara, California 93106, United States

‡Energy Storage and Distributed Resources Division, Lawrence Berkeley National Laboratory,

Berkeley, CA 94720

¶Materials Department, University of California, Santa Barbara, California 93106, United
States

§X-ray Sciences Division, Argonne National Laboratory, Lemont, Illinois 60439

||Materials Science and Engineering, University of California, Berkeley, CA 94 720

\(\to\$Department of Chemistry and Biochemistry, Santa Barbara, California 93106, United States

E-mail: seshadri@mrl.ucsb.edu

Table S1: Compositional analysis of  $Mn_{1+x}Sb$  samples from scanning electron microscopy analysis

nominal x	Average Mn (weight percent)	Average Mn (moles)
0.0	49.7(6)	0.99(1)
0.1	51.3(3)	1.027(6)
0.2	53.9(2)	1.078(4)

Table S2: Unit cell parameters,  $R_{wp}$  values, and impurity phase fractions from Rietveld refinement of synchrotron X-ray diffraction data for  $\mathrm{Mn}_{1+x}\mathrm{Sb}$ 

x	a (Å)	b (Å)	V (Å <sup>3</sup> )	$R_w p$	Mn <sub>2</sub> Sb(% wt)
0.0 (phase 1)	4.1448(2)	5.7771(4)	86.619(1)	17.94	_
0.0 (phase 2)	4.1357(2)	5.7858(4)	85.702(1)		
0.1 (phase 1)	4.1693(2)	5.7535(3)	86.616(1)	18.46	
0.1 (phase 2)	4.1698(2)	5.7524(3)	86.619(1)		
0.2 (phase 1)	4.2231(1)	5.7103(2)	88.199(1)	14.59	2.4(5)
0.2 (phase 1)	4.2158(2)	5.7154(6)	87.969(1)		

Table S3: Magnetic properties of  $Mn_{1+x}Sb$ 

x	$T_C$ (K) <sup>a</sup>	$M_{sat}^b (\mu_B)$	$M_{sat} (\mu_B)$	$\Sigma_M$ (%)	$ \Delta S_M  (\text{J K}^{-1} \text{ kg}^{-1})^c$	RC (J kg <sup>-1</sup> )
0	561	3.1	3.4	5.9	3.6	265
0.1	491	2.9	2.8	4.5	3.0	268
0.2	338	2.6	1.9	3.7	2.8	200

<sup>&</sup>lt;sup>a</sup>As determined by the Arrott method.

<sup>&</sup>lt;sup>b</sup>Calculated by DFT

 $<sup>^{</sup>c}\Delta H = 0$  T to 5 T.

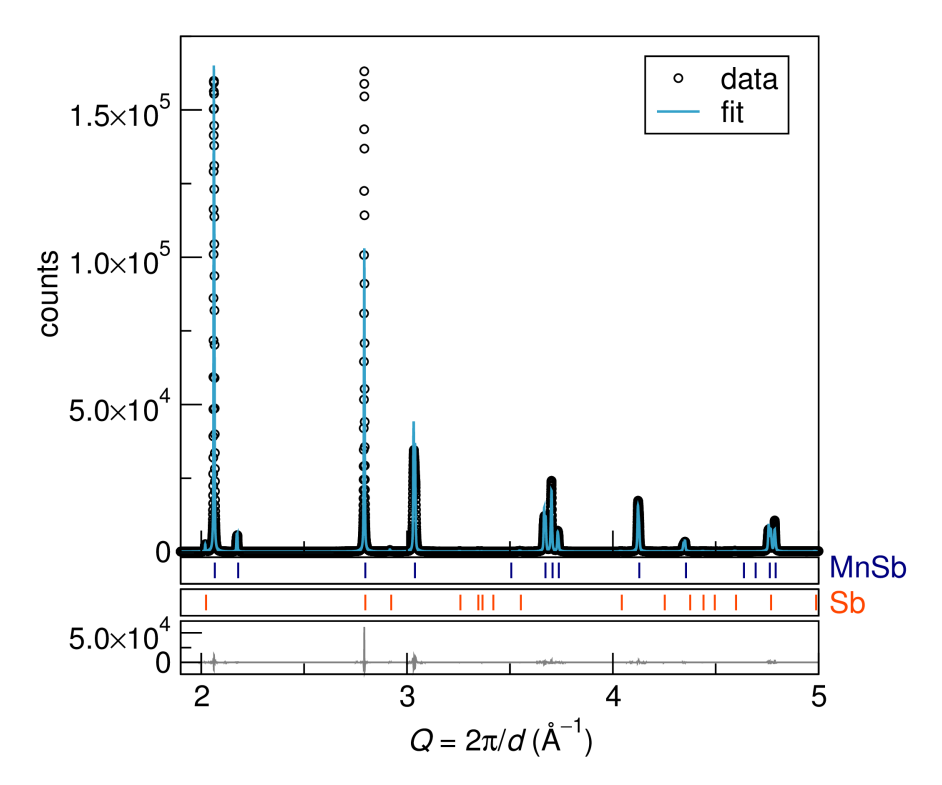


Figure S1: The Rietveld refinement of x=0.0 is shown, with hkl ticks of the main phase and the impurity, Sb, shown below the pattern. The difference curve is shown in the bottom panel.

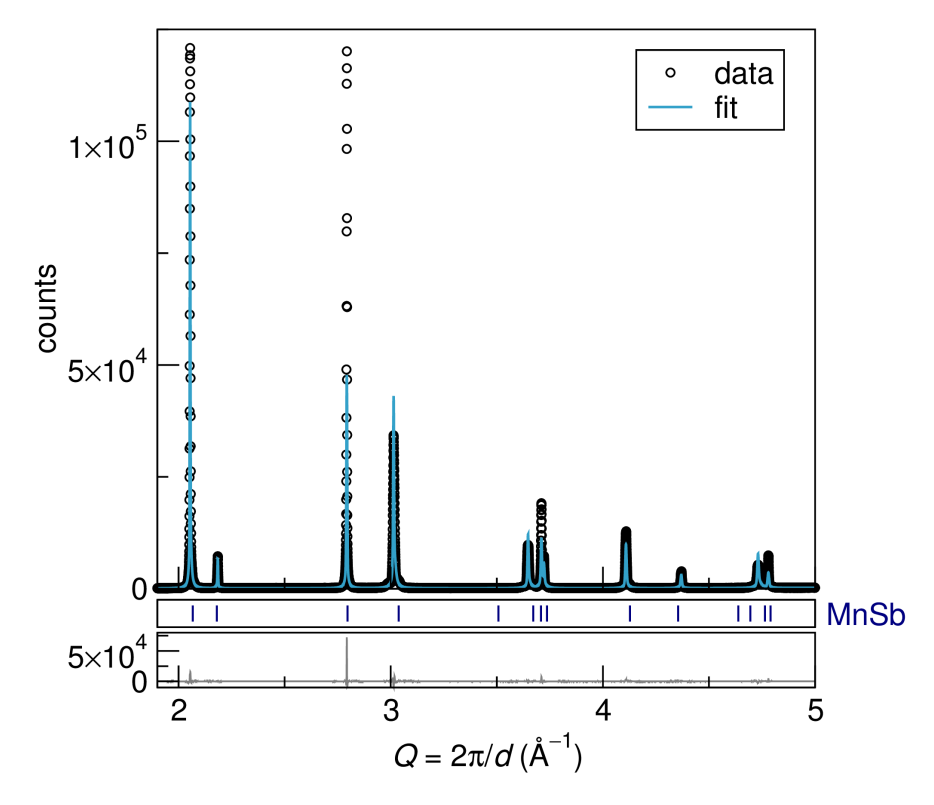


Figure S2: The Rietveld refinement of x=0.1 is shown, with hkl ticks of the main phase shown below the pattern. The difference curve is shown in the bottom panel.

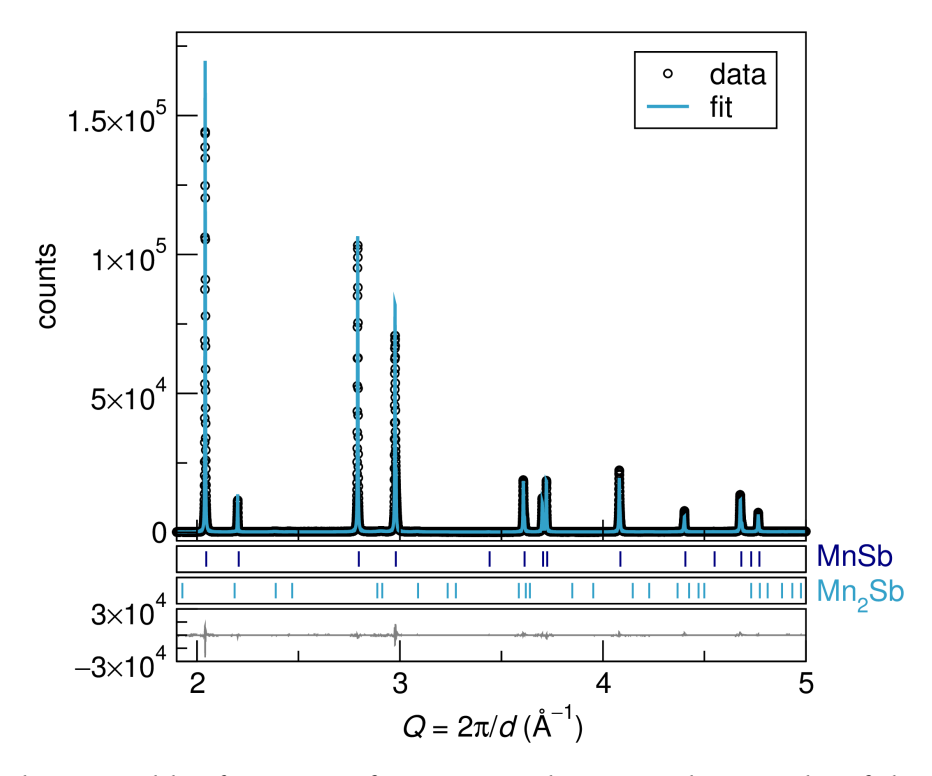


Figure S3: The Rietveld refinement of x = 0.2 is shown, with hkl ticks of the main phase and the impurity,  $Mn_2Sb$ , shown below the pattern. The difference curve is shown in the bottom panel.

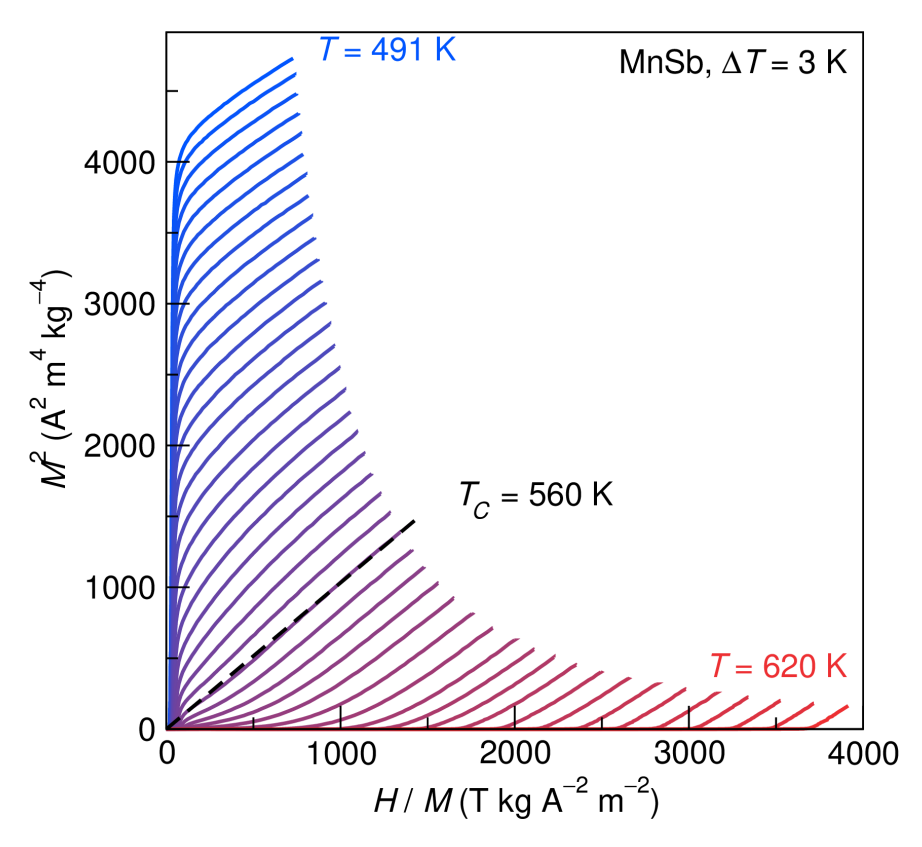


Figure S4: Field-dependent magnetization isotherms of x=0.0 are plotted in the Arrott style to emphasize the true  $T_C$  near 560 K.

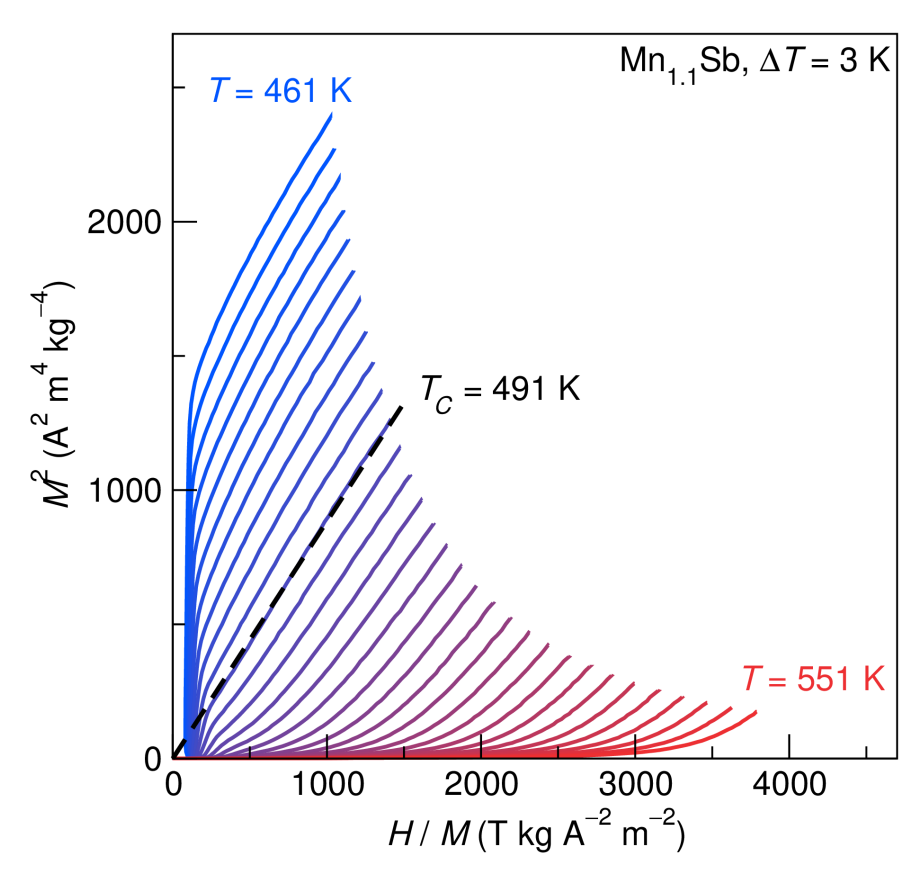


Figure S5: Field-dependent magnetization isotherms of x=0.1 are plotted in the Arrott style to emphasize the true  $T_C$  near 491 K.

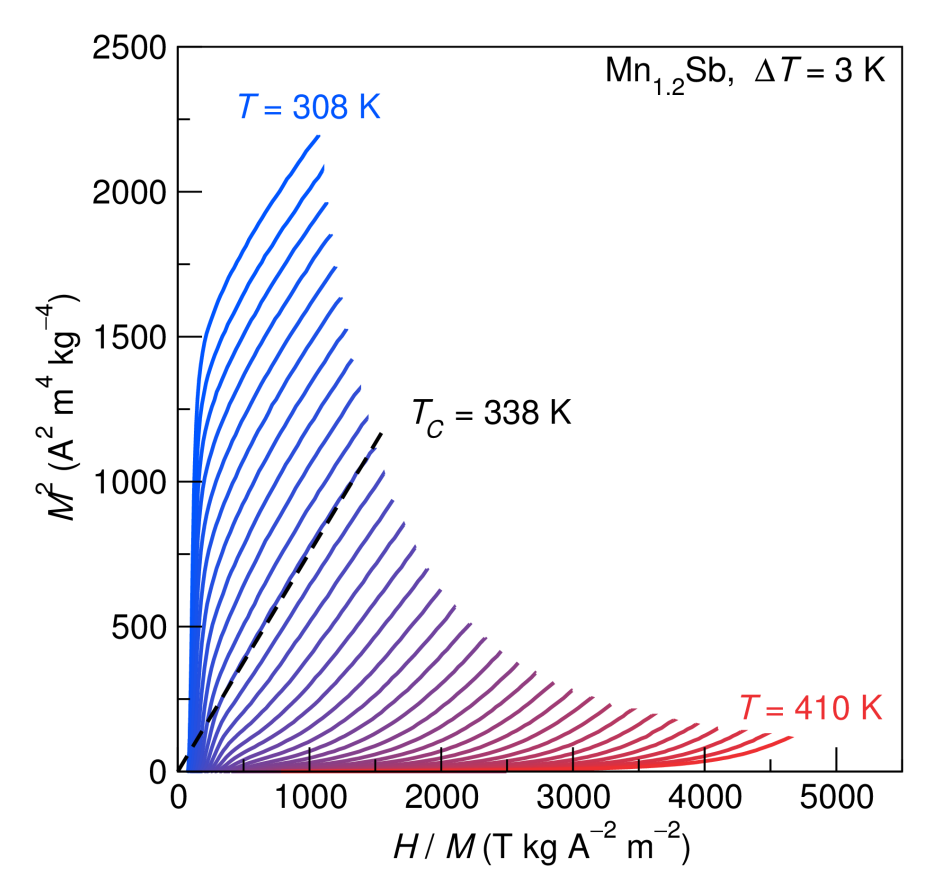


Figure S6: Field-dependent magnetization isotherms of x=0.0 are plotted in the Arrott style to emphasize the true  $T_C$  near 338 K.

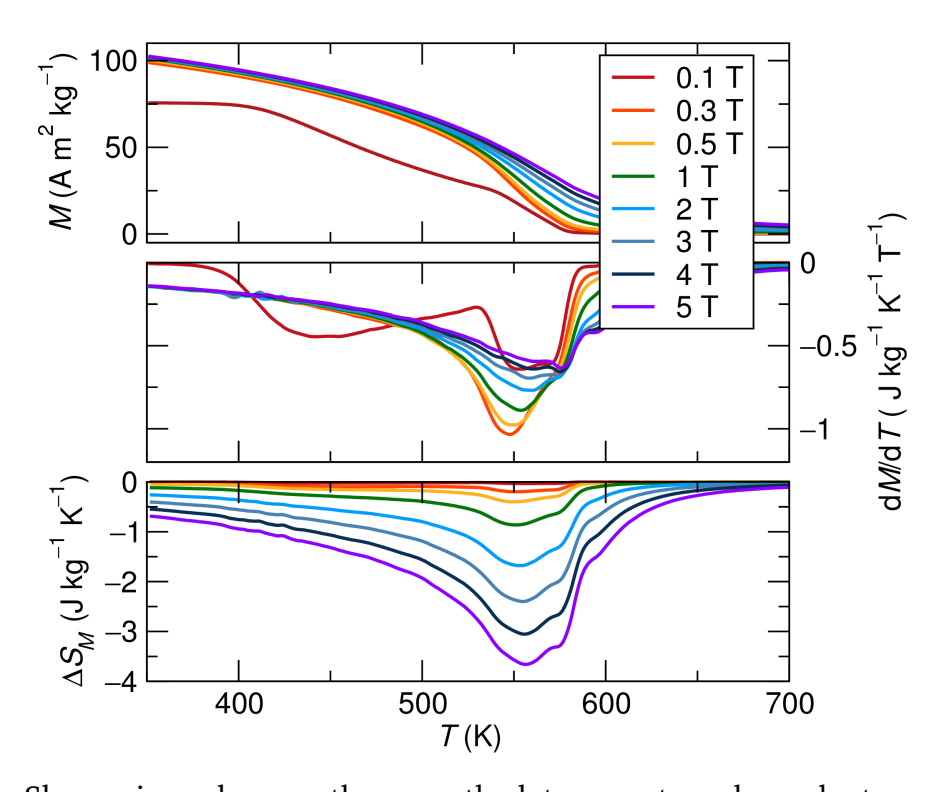


Figure S7: Shown in order are the smoothed temperature-dependent magnetization, derivatives, and  $\Delta S_M$  curves for x=0.0.

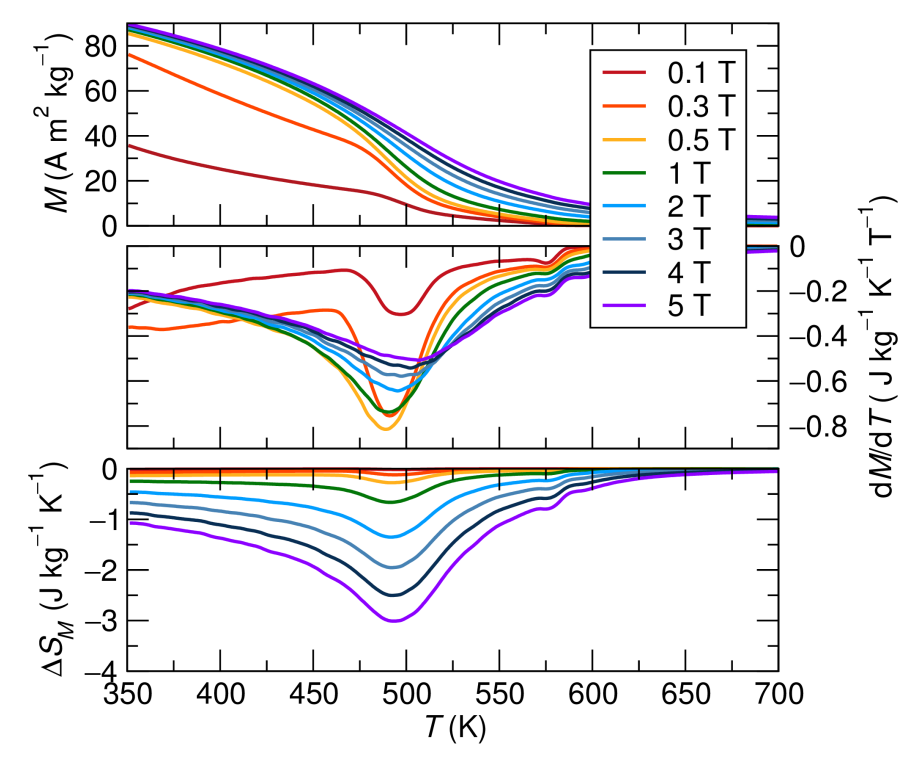


Figure S8: Shown in order are the smoothed temperature-dependent magnetization, derivatives, and  $\Delta S_M$  curves for x=0.1.

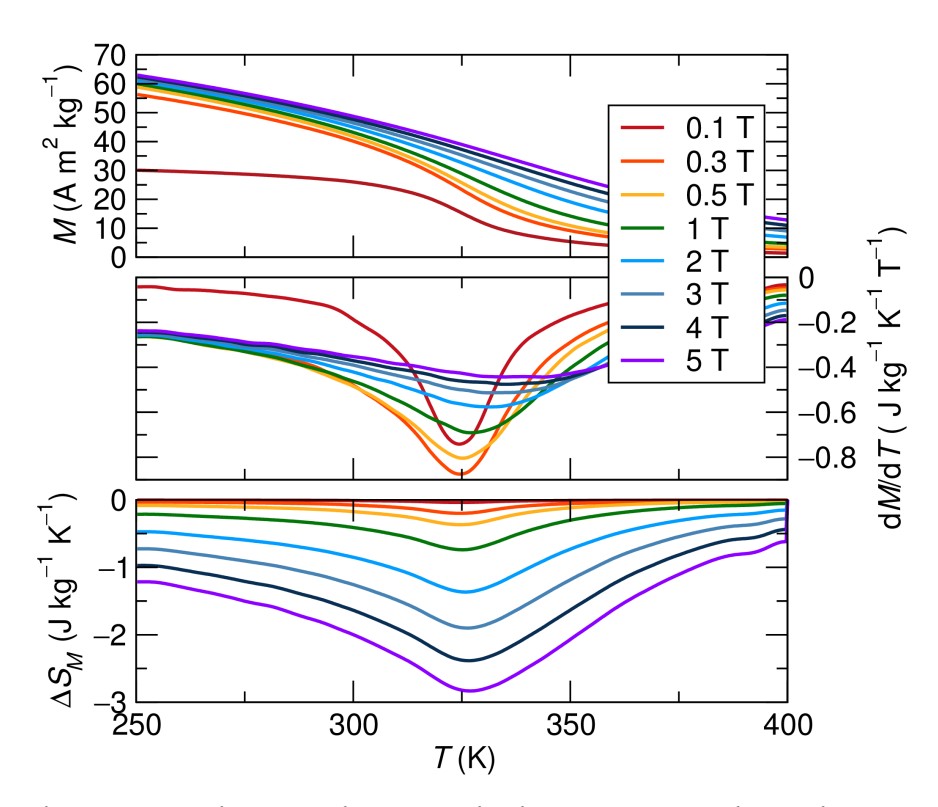


Figure S9: Shown in order are the smoothed temperature-dependent magnetization, derivatives, and  $\Delta S_M$  curves for x= 0.2.